uc3m | Universidad Carlos III de Madrid

e-Archivo

This is a postprint version of the published document at:

Rodríguez-Millán, M., Vaz-Romero, A., Rusinek, A., Rodríguez-Martínez, J. A. y Arias, A. (2014). Experimental Study on the Perforation Process of 5754-H111 and 6082-T6 Aluminium Plates Subjected to Normal Impact by Conical, Hemispherical and Blunt Projectiles. *Experimental Mechanics,* 54, pp. 729–742.

DOI: https://doi.org/10.1007/s11340-013-9829-z

© 2013 Society for Experimental Mechanics.

Experimental Study on the Perforation Process of 5754-H111 and 6082-T6 Aluminium Plates Subjected to Normal Impact by Conical, Hemispherical and Blunt Projectiles

M. Rodríguez-Millán · A. Vaz-Romero · A. Rusinek · J.A. Rodríguez-Martínez · A. Arias

Abstract This paper presents an experimental investigation on the perforation behaviour of 5754-H111 and 6082-T6 aluminium alloys. The mechanical response of these materials has been characterized in compression with strain rates in the range of $10^{-3}\ s^{-1} < \dot{\varepsilon} < 5 \cdot 10^{3}\ s^{-1}$. Moreover, penetration tests have been conducted on 5754-H111 and 6082-T6 plates of 4 mm thickness using conical, hemispherical and blunt projectiles. The perforation experiments covered impact velocities in the range of $50\ m/s < V_0 < 200\ m/s$. The initial and residual velocities of the projectile were measured and the ballistic limit velocity obtained for the two aluminium alloys for the different nose shapes. Failure mode and post-mortem deflection of the plates have been examined and the perforation mechanisms associated to each projectile/target configuration investigated. It has been shown that the energy absorption capacity of the impacted plates is the result of the collective role played by target material behaviour, projectile nose shape and impact velocity in the penetration mechanisms.

M. Rodríguez-Millán · A. Vaz-Romero · A. Arias
Department of Continuum Mechanics and Structural Analysis, University Carlos III of Madrid, Avda. de la Universidad 30, 28911 Leganés, Madrid, Spain

A. Rusinek
Laboratory of Mechanics, Biomechanics, Polymers and Structures (LaBPS), National Engineering School of Metz (ENIM), 1 route dArs Laquenexy, 57078 Metz Cedex 3, France

J.A. Rodríguez-Martínez (✉)
Department of Continuum Mechanics and Structural Analysis, University Carlos III of Madrid, Avda. de la Universidad 30, 28911 Leganés, Madrid, Spain
e-mail: jarmarti@ing.uc3m.es

Keywords AA 5754-H111 · AA 6082-T6 · Perforation · Ballistic limit · Energy absorption

Introduction

Impact and blast threats exist in a wide range of engineering, security and defence sectors. The protection of civil infrastructures and critical industrial facilities are topics of increasing relevance to defence agencies and governments. In the transport industry, energy absorption and crashworthiness are key points in the design process of vehicles, vessels and aircrafts. Development of protective structures capable of sustaining an impact keeping the structural integrity is thus one of the main challenges of modern industry. In the design and development of structural solutions suitable for energy absorption under impact loading, the material selection represents a crucial decision.

Within this framework, large efforts have been directed in automotive, shipping and aircraft industries toward the development of light-weight alloys (aluminium, magnesium and titanium alloys) for high-performance dynamic applications. Enhanced by the increasing restrictions in fuel consumption and the encouragement for emissions reduction, there is an emerging trend to replace the conventional Fe-based materials by these non-ferrous alloys in transportation industry applications [1–5]. In particular, in the automotive sector, aluminium alloys are now widely used in the manufacture of structural parts responsible for energy absorption and crashworthiness [6–8]. The goal being to develop passive safety of vehicles through structures fabricated using materials with the highest possible strength-to-weight ratio.

Important steps in this direction have been taken over the last two decades and a vast body of literature has been

published on the mechanical behaviour of different aluminium alloys, see for example [9–12]. Within this context, our interest is focussed on the experimental assessment of aluminium plate products as energy absorbers in dynamic penetration processes. It is worth noting a number of relevant works published in this field by different authors [13–22]. Primary interest in these papers is determining the parameters affecting the ballistic capacity of the target. The purpose is to correlate the penetration mechanisms with the governing variables of the problem: target and projectile characteristics (geometrical and mechanical) and actual impact conditions (impact velocity).

The investigation reported in the present paper is precisely of this nature. Firstly, the mechanical behaviour of 5754-H111 and 6082-T6 aluminium alloys is characterized in compression with strain rates in the range of $10^{-3}\ s^{-1} < \dot{\varepsilon} < 5 \cdot 10^{3}\ s^{-1}$. Secondly, normal perforation tests on 5754-H111 and 6082-T6 plates of 4 mm thickness are conducted using conical, hemispherical and blunt projectiles with impact velocities in the range of $50\ m/s < V_0 < 200\ m/s$. The goal is to illustrate the joint effect that target material behaviour, projectile nose shape and impact velocity have on the penetration mechanisms. From the analysis emerge two main ideas, which are the main innovative features of this paper: (1) the penetration efficiency of a given nose shape with regard to the others depends on the material target and (2) the suitability for energy absorption of a given target material with regard to other depends on projectile shape and impact velocity.

Materials

The aluminium wrought alloys investigated are 5754-H111 and 6082-T6.

Aluminium alloy 5754 is a medium strength alloy with excellent corrosion resistance especially to seawater and industrially polluted atmospheres. H111 implies that the alloy is work hardened by shaping processes. Aluminium alloy 5754-H111 shows good cold formability, high fatigue strength and fair machinability. It is within the alloys of the 5xxx series of higher strength. This makes 5754-H111 highly suited to flooring applications, shipbuilding or chemical and nuclear structures. It is also commonly used for automotive structural members and inner body panels. The chemical composition of the material (% of weight) is reported in Table 1.

Aluminium alloy 6082 is a medium strength alloy with remarkable corrosion resistance. T6 implies that the alloy is heat treated and artificially aged. It has the highest strength of the 6xxx series. Aluminium alloy 6082-T6 shows excellent performance in machining operations. This grade substitutes to the conventional 6061 alloy in many structural applications in which improved mechanical properties are required. It is widely used in transport and structural applications in which high stress resistance is essential. It can be found in the exterior of the planes fuselages and it is a real alternative to conventional mild steel in automotive body panels and structures. The chemical composition of the material (% of weight) is reported in Table 2.

Table 1 Chemical composition of the AA5754-H111 (% of weight)

Mn	Si	Cr	Cu	Zn	Fe	Ti	Mg
0.26	0.29	0.03	0.04	0.02	0.32	0.03	2.80

In order to reveal the mechanical behaviour of both alloys under impact loading conditions, the flow characteristics of the materials as function of strain rate have been investigated.

Compressive Viscoplastic Response of 5754-H111 and 6082-T6 Aluminum Alloys under Wide Ranges of Strain Rate at Room Temperature

Specimens used to perform the compression tests and targets used in the perforation experiments (see section "Perfo ration Experiments") were machined from the same plates. The cylindrical compression samples, considered in both quasi-static and dynamic tests, had the following dimensions: diameter $\phi = 8\ mm$ and thickness $t = 4\ mm$. The loading direction is the one corresponding to the thickness of the plates. According to the considerations reported elsewhere [24–27] the aspect ratio $\phi/t = 2.0$ prevents from significant friction and inertia effects. Additionally, sample ends were lubricated to reduce friction effects during the tests.

Quasi-Static Compression Tests

Low-rate compression tests were conducted using a servo-electric testing machine within the range of strain rates $10^{-3}\ s^{-1} < \dot{\varepsilon} < 10^{-1}\ s^{-1}$. Figure 1 shows representa-tive quasi-static compression stress-strain curves for both materials tested. The magnitude of rate sensitivity is negli-gible for both alloys within this range of strain rates, which

Table 2 Chemical composition of the AA6082-T6 (% of weight)

Mn	Si	Cr	Ni	Cu	Zn	Fe	Ti	Mg
0.45	0.99	0.03	0.01	0.08	0.04	0.41	0.03	0.73

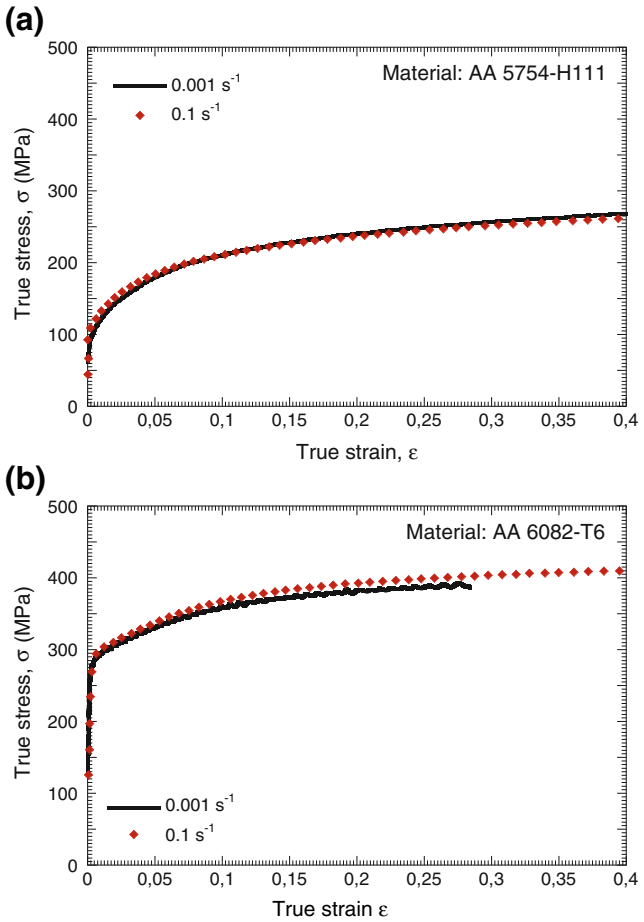

Fig. 1 Representative quasi-static compression stress-strain curves. (**a**) AA 5754-H111 and (**b**) AA 6082-T6

is a common characteristic shared by many commercial aluminium alloys [28]. Furthermore, within this range of strain rates the strain hardening exhibits almost negligible dependence on the loading rate for both alloys investigated.

Moreover, Fig. 1 reveals that the AA 6082-T6 displays larger yield stress whereas the AA 5754-H111 shows greater strain hardening. The latter observation is highlighted in Fig. 2 which shows, for both materials tested, the strain hardening $\theta = \partial\sigma/\partial\varepsilon$ versus the normalized flow stress $Y = \sigma/\sigma_0$, being σ_0 the material yield stress at the onset of plastic deformation. The remarkable strain hardening dis-played by the AA 5754-H111 boosts the material flow stress and delays the flow saturation condition ($\theta = 0$). The AA 5754-H111 is therefore expected to show greater ductility than the AA 6082-T6, as it will be discussed in forthcoming sections of this paper.

Dynamic Compression Tests

High-rate compression experiments with strain rates in the range $7.5 \cdot 10^2\, s^{-1} < \dot{\varepsilon} < 5 \cdot 10^3\, s^{-1}$ were carried out using

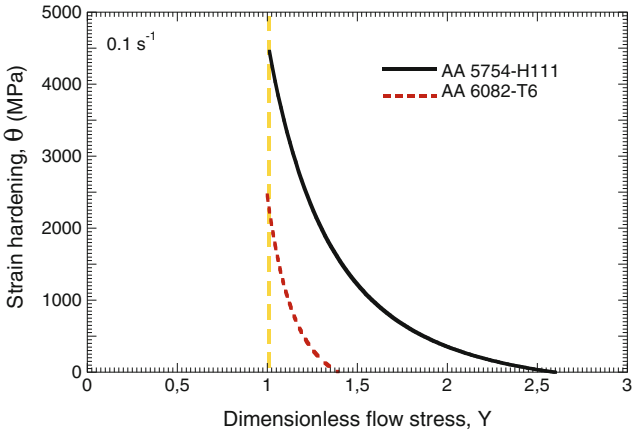

Fig. 2 Representative experimental results: strain hardening θ versus dimensionless flow stress Y for both materials tested

a conventional Kolsky apparatus (Split Hopkinson Pressure Bar) made of high strength steel, which exhibits higher yield stress $\sigma_y \approx 1000\ MPa$ than that of the materials tested under dynamic conditions of deformation. Detailed information about the experimental arrangement can be found in previous work of authors [25]. Note that in order to determine the stress-strain curves, dynamic specimen equilibrium (force equilibrium, energy balance) was verified for each sample, and corrections for wave dispersion and friction effects were applied using a home-made program [29] according to the conventional wave analysis.

Figure 3 shows representative dynamic compression stress-strain curves for AA 5754-H111 and AA 6082-T6. As previously determined from the low-rate experiments, the strain hardening of both materials is nearly independent of the loading rate. Moreover, it has to be noted that the flow stress of both 5754-H111 and 6082-T6 slightly increased in comparison with the value observed in the low-rate tests.

Figure 4 illustrates the flow stress at strain equal to 0.1 versus the strain rate for both materials analysed. The experiments conducted in this work are plotted together with those reported elsewhere [7, 28, 30, 31]. The flow stress is largely strain rate insensitive until $\dot{\varepsilon} \approx 10^3\, s^{-1}$. Beyond that loading rate both materials show an incipient strain rate sensitivity. This observation is consistent with the experimental evidence reported elsewhere [26, 28, 32–34] where it is shown that most commercial aluminium alloys exhibit increasing rate sensitivity once a threshold loading rate (typically within $10^3 - 10^4 s^{-1}$) is exceeded.

Perforation Experiments

The tested square plates were $A_0 = 130 \times 130\ mm^2$ with a thickness of 4 mm. Their active surface area, after they

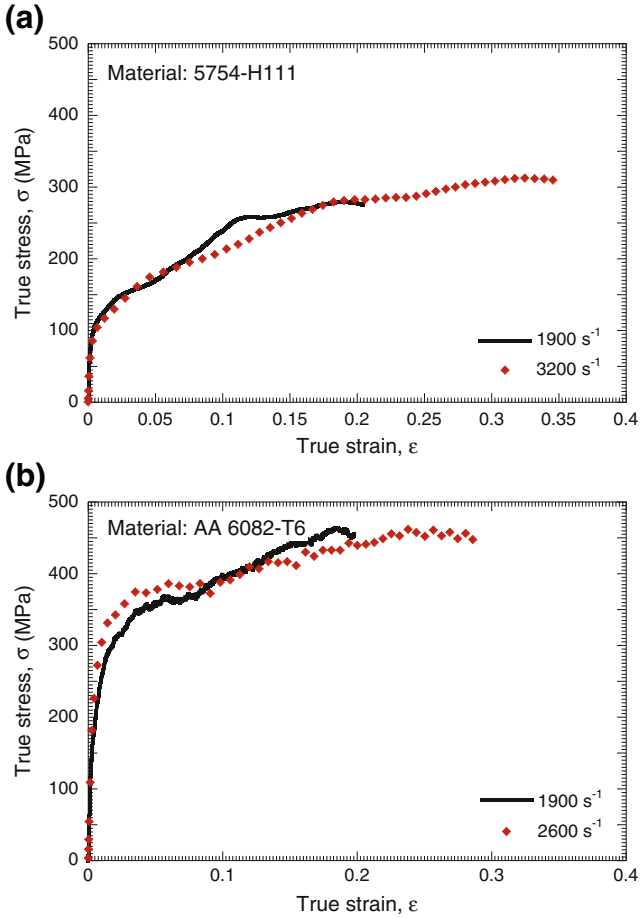

Fig. 3 Representative dynamic compression stress-strain curves. (**a**) Material: AA 5754-H111. (**b**) Material: AA 6082-T6

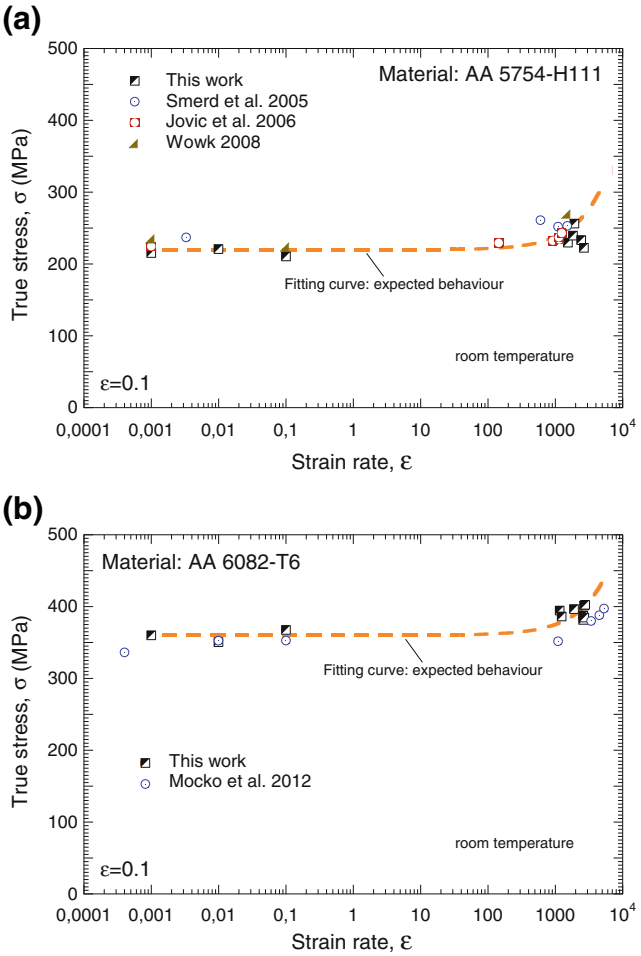

Fig. 4 Flow stress upon strain rate for $\varepsilon = 0.1$. (**a**) Material: AA 5754-H111. (**b**) Material: AA 6082-T6

were screwed and clamped to the support, was $A_f = 100 \times 100\ mm^2$. The plate is embedded on a rigid support in such a way that sliding effects are avoided during the impact tests. This arrangement (screwing + clamping) used to fix the plates in the impact tests has been proven to be effective avoiding any slippage at the supports as discussed in previous works of the authors [35, 36].

Conical, hemispherical and blunt projectiles were used in the perforation tests. Their geometries and dimensions are shown in Fig. 5. In order to preserve the same initial kinetic energy, the masses of the projectiles were constant: $M_p = 30\ g$. The projectiles were machined using maraging steel, which exhibits higher yield stress – $\sigma_y \approx 2000\ MPa$ – than that of the materials tested under dynamic conditions of deformation. In addition, the projectiles underwent a heat treatment to increase their hardness.

To perform perpendicular impact tests on the aluminium plates, a pneumatic gas gun was used. It should be noticed that the diameter of the barrel was roughly equal to the diameter of the projectiles. No sabot was required for guidance of the projectile inside the barrel, which helps to ensure the perpendicularity of the impact.

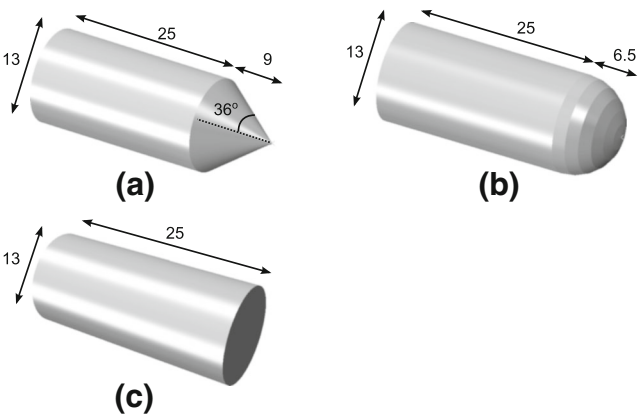

Fig. 5 Geometry and dimensions (*mm*) of the projectiles used in the perforation tests. (**a**) Conical projectile. (**b**) Hemispherical projectile. (**c**) Blunt projectile

The impact velocity, V_0, and the residual velocity, V_r, were measured using lasers coupled to photodiodes and time counters. When the projectile passes through the laser beam, a time counter is triggered. This procedure is repeated twice (twice before the impact and twice after), defining the time interval. Then, the impact velocity $V_0 = \frac{\Delta X_{12}^{laser}}{\Delta t_{12}}$, and the residual velocity $V_r = \frac{\Delta X_{34}^{laser}}{\Delta t_{34}}$ are determined, where ΔX_{ij}^{laser} is the predetermined distance between the lasers and Δt_{ij} is the recorded time interval. Further details of the experimental setup can be found in previous works by the authors, see [36, 37]. Perforation experiments were performed with impact velocities in the range of $50\ m/s < V_0 < 200\ m/s$. It should be noted that, for all the tests performed, the projectiles showed an absence of plastic straining, damage or erosion after the impact. Next, the experimental results are discussed.

Conical Projectile Configuration

Firstly, the results obtained using the conical projectile configuration are analysed. Figure 6 shows the residual velocity versus impact velocity ($V_r - V_0$) curves obtained for both materials tested. The ballistic limit of the AA 5754-H111 plates – $V_{bl} \approx 147\ m/s$ – was found to be just slightly greater than that corresponding to the AA 6082-T6 plates – $V_{bl} \approx 143\ m/s$ – . The results shown in Fig. 6 have been fitted via the expression proposed by Recht and Ipson [38]

$$V_r = \left(V_0^{\kappa} - V_{bl}^{\kappa}\right)^{1/\kappa} \tag{1}$$

where κ is a fitting parameter. The values of κ determined were $\kappa = 1.95$ for the AA 5754-H111 and $\kappa = 1.88$ for the AA 6082-T6. The energy absorbed by the target within the range of impact velocities tested is largely similar for both materials tested. Particularly, for initial velocities larger than $\sim 170\ m/s$ both materials display practically identical $V_r - V_0$ relation. It was noted that the flow stress of AA 6082-T6 is about 50 % higher than that for 5754-H111 alloy. However, due to the lower fracture toughness of the AA 6082-T6, the two materials show much closer $V_r - V_0$ relations than expected based on the difference in strength. This suggests that the energy absorption mechanisms shown by both materials investigated are largely different to each other.

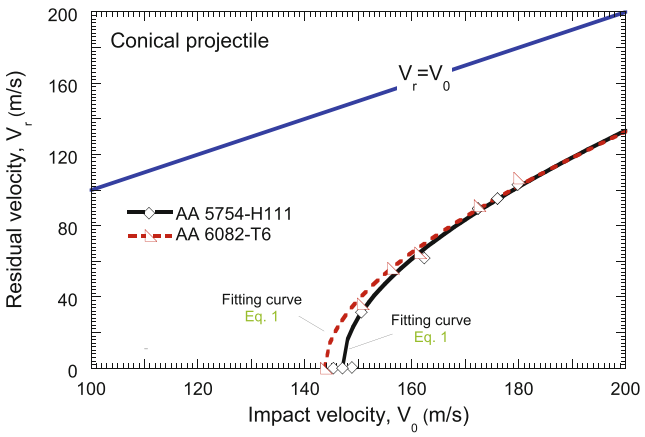

Fig. 6 Conical projectile configuration. Residual velocity V_r versus impact velocity V_0. Comparison between AA 5754-H111 and AA 6082-T6

Figures 7 and 8 illustrate the final stage of the impact process for different initial velocities and both materials tested.

During the perforation of the AA 5754-H111 plates the projectile pushes the material target to the side, causing radial flow (ductile hole formation), target bending and subsequent formation of symmetric petals (see [39]). The number of petals varied between three and five for all the tests performed. Three or four petals are formed at impact velocities close to the ballistic limit whereas five petals are observed for the higher loading velocities tested. The increasing number of petals with impact velocity is caused by the enhanced role played by inertia in the perforation mechanisms as the loading rate increases. Inertia boosts the dominant wavenumber, which dictates the distance between localization points [40–42], being such localization points precursors of the onset of radial cracks which trigger the petals formation. It should be noted that this number of petals (from 3 to 5) is frequently reported in the literature [43–45] for boundary value problems involving perforation of ductile metallic sheets by conical projectiles at low/intermediate impact velocities. This recurring number of petals is correlated to a minimum of the total rate of energy dissipation (i.e. to the dominant wavenumber, see [42, 46] for further details) as explained elsewhere [47, 48]. Large plastic membrane stretching and permanent bending are observed in the impacted plates, Fig. 9. The kinetic energy of the projectile is absorbed by a combination of local and structural impact mechanisms.

The failure mode of the AA 6082-T6 plates is clearly different from that observed in the AA 5754-H111 targets. During the perforation process the material ahead of the projectile is bulged rearward (see [39]). In comparison with the 5754-H111 plates, plastic membrane stretching and permanent bending are smaller, Fig. 9. A debris cloud constituted by multiple fragments is ejected during the perforation process which precludes the formation of developed petals. Noticeable fragmentation confirms that the ductility of the AA 6082-T6 is markedly lower than that of the AA 5754-H111. In contrast with the observations reported for the AA

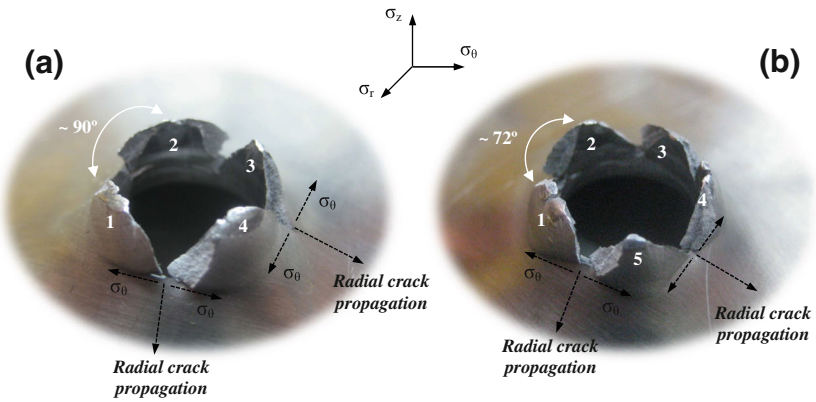

Fig. 7 Conical projectile configuration. Material: AA 5754-H111. Final stage of the perforation process for different impact velocities. (**a**) $V_0 = 148.81\ m/s$. (**b**) $V_0 = 179.86\ m/s$

5754-H111 plates, the local impact mechanisms are more important in the process of energy absorption.

Hemispherical Projectile Configuration

The results obtained using the hemispherical projectile configuration are analysed. Figure 10 shows the residual velocity versus impact velocity $(V_r - V_0)$ curves obtained for both materials tested. The ballistic limit was found to be $V_{bl} \approx 166\ m/s$ for the AA 5754-H111 plates and $V_{bl} \approx 137\ m/s$ for the AA 6082-T6 targets. The results shown in Fig. 6 have been fitted using equation (1). The values of κ determined were $\kappa = 2.17$ for the AA 5754-H111 and $\kappa = 2.08$ for the AA 6082-T6. For the whole range of impact velocities tested the AA 5754-H111 plates display greater capacity for energy absorption than the AA 6082-T6 samples. Unlike what observed in the case of the conical projectile config-uration, the ballistic limit velocity notably varies with the material tested. It should be noticed that, with regard to the conical projectile configuration, the ballistic limit for the AA5754-H111 has increased whereas for the AA6082-T6 has slightly decreased. The effect of varying the nose shape on the $(V_r - V_0)$ curves depends on the material target.

Figure 11 illustrates the final stage of the impact process for both materials tested. Post-mortem analysis of the impacted plates reveals different failure mechanisms depending on the material tested.

The perforation process of the AA 5754-H111 plates is characterized by ductile hole formation. During perforation, large plastic flow occurs in the vicinity of the penetrating projectile. The moving projectile pushes the material, aside radially and forward. Discing and plate thinning occur which lead to severe localised rear bulging and subsequent necking. Necking takes place close to the dome of the projectile/plate contact area leading to the ejection of a severely deformed cup-shaped plug. The thickness and the diameter of the plug are smaller than the thickness of the plate and the diameter of the projectile respectively. An extended zone subjected to plastic membrane stretching and large bending is seen in the impacted plates, Fig. 12. The struc-tural effects are key factor in the energy absorption process. This type of failure mode is characterized by high energy consumption [49].

The failure mode of the AA 6082-T6 plates is different from that observed in the AA 5754-H111 plates. The penetrator pushes forward the material target located ahead of

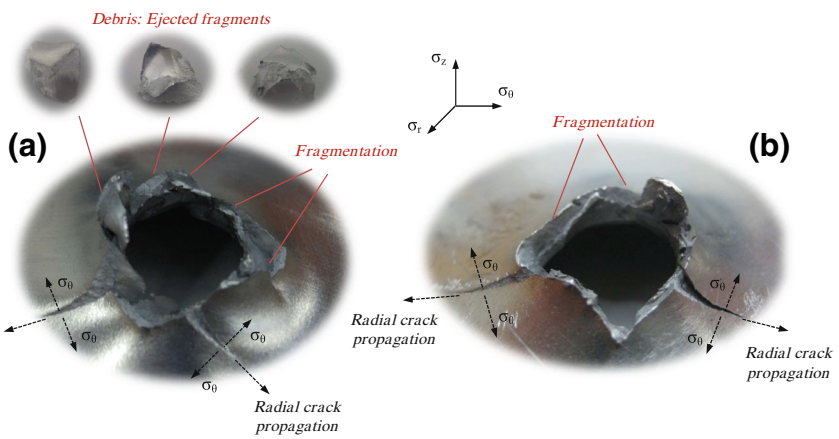

Fig. 8 Conical projectile configuration. Material: AA 6082-T6. Final stage of the perforation process for different impact velocities. (**a**) $V_0 = 143.68\ m/s$. (**b**) $V_0 = 150.60\ m/s$

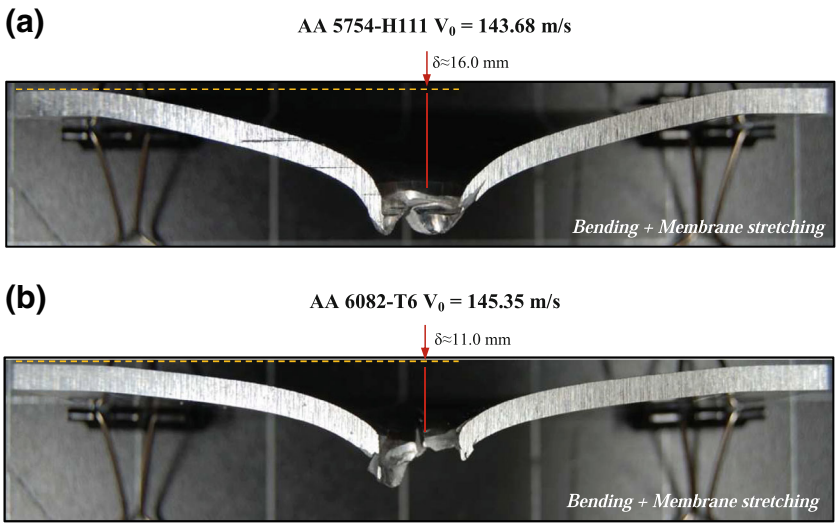

Fig. 9 Conical projectile configuration. Cross-sections of penetrated plates. Both plates are tested at largely similar impact velocities. (**a**) Material: AA 5754-H111. $V_0 = 143.68\ m/s$. (**b**) Material: AA 6082-T6. $V_0 = 145.35\ m/s$

the projectile leading to the formation of shear bands that progress through the thickness of the plate until they reach the rear side of the target, Fig. 12(b). A circular plug which barely shows traces of plastic deformation is formed. The thickness and the diameter of the plug are largely close to the thickness of the plate and the diameter of the projectile respectively. The noticeable yield stress level of this material hinders discing and target thinning which makes to the AA 6082-T6 plates prone to shear band formation. In comparison with the 5754-H111 plates, plastic membrane stretching and permanent bending are largely shorter, Fig. 12. Localised rear bulging with radial cracks and short petals is seen. These observations evidence that local effects play a major role in the energy absorption process for 6082-T6 plates.

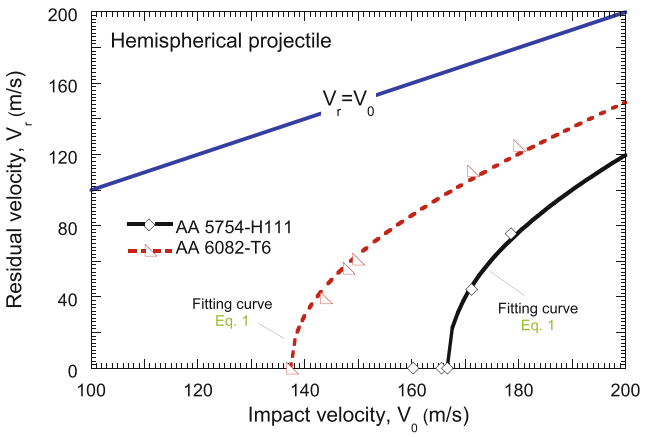

Fig. 10 Hemispherical projectile configuration. Residual velocity V_r versus impact velocity V_0. Comparison between AA 5754-H111 and AA 6082-T6

Blunt Projectile Configuration

The results obtained using the blunt projectile configuration are analysed. Figure 13 shows the residual velocity versus impact velocity ($V_r - V_0$) curves obtained for both materials tested. The ballistic limit was found to be $V_{bl} \approx 120\ m/s$ for the AA 5754-H111 plates and $V_{bl} \approx 129\ m/s$ for the AA 6082-T6 targets. Note that these values are smaller than those measured for the conical and hemispherical projectile configurations. The results shown in Fig. 6 have been fitted using equation (1). The values of κ determined were $\kappa = 2.09$ for the AA 5754-H111 plates and $\kappa = 2.77$ for the AA 6082-T6 targets. Unlike what observed in the case of the conical and hemispherical projectile configurations, the lower ballistic limit corresponds to the AA 5754-H111 plates. However, it should be noted that the superior capacity for energy absorption of the AA 6082-T6 plates is limited to certain range of impact velocities. At velocities above $\sim 135\ m/s$ the AA 5754-H111 plates display higher capacity for energy absorption.

Figure 14 illustrates the final stage of the impact process for both materials tested. Post-mortem analysis of the impacted plates reveals different failure mechanisms depending on the material tested.

The perforation process of the AA 5754-H111 plates is a combination of discing and shear banding [19, 39]. Shear bands formation and progression occurs after thinning of the localised region, Fig. 15(a). The thickness of the ejected plug is slightly smaller than the thickness of the plate. Post-mortem observations reveal membrane stretching and plastic bending of the impacted samples, Fig. 15. The kinetic energy of the projectile is absorbed by a combination of local and structural impact mechanisms.

The failure mode of the AA 6082-T6 plates is fully controlled by shear banding which leads to the ejection of a

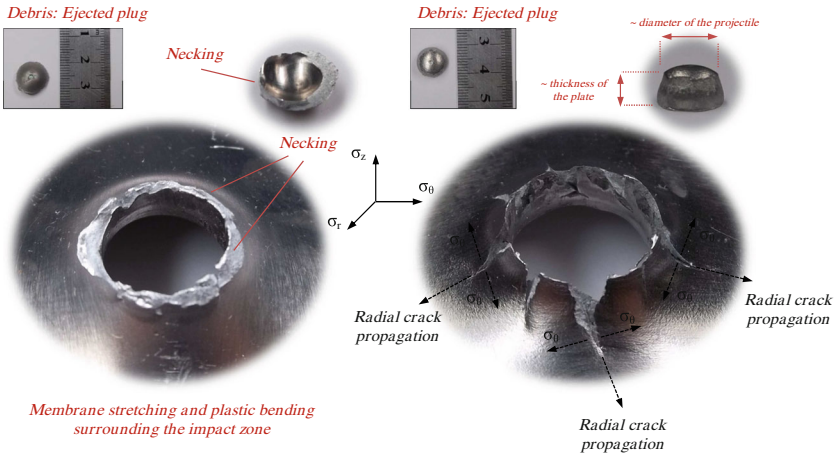

Fig. 11 Hemispherical projectile configuration. Final stage of the perforation process. (**a**) Material: AA 5754-H111. $V_0 = 166.67\ m/s$. (**b**) Material: AA 6082-T6. $V_0 = 179.86\ m/s$

circular plug as the final stage of the perforation process. The perforation time is very small, the target material is shortly pushed in front of the projectile before shear localisation occurs, Fig. 15(b). Shear bands are formed without noticeable thinning of the localised region. The thickness of the ejected plug is largely similar to the original thickness of the plate. The projectile causes clean cuts in the plates giving a sharp indentation of the target. Just a modest (smooth) bulge is obtained in the rear side of the penetrated plates. In comparison with the 5754-H111 targets, very limited discing and plastic bending is observed, Fig. 15. Very little plastic deformation appear outside the localised shear zone. The kinetic energy of the projectile is absorbed by local impact mechanisms.

The different perforation mechanisms displayed by both material targets seems to justify the intersection of the $V_r - V_0$ curves illustrated in Fig. 13. The larger ballistic limit of the 6082-T6 is attributed to its larger yield stress which enhances the critical impact velocity required for the shear bands formation. However, once the ballistic limit is exceeded, the energy consumed by this failure mechanism considerably decreases as the impact velocity increases (at least within the rage of impact velocities tested as it will be shown in section "Discussion"). Thus, at high impact

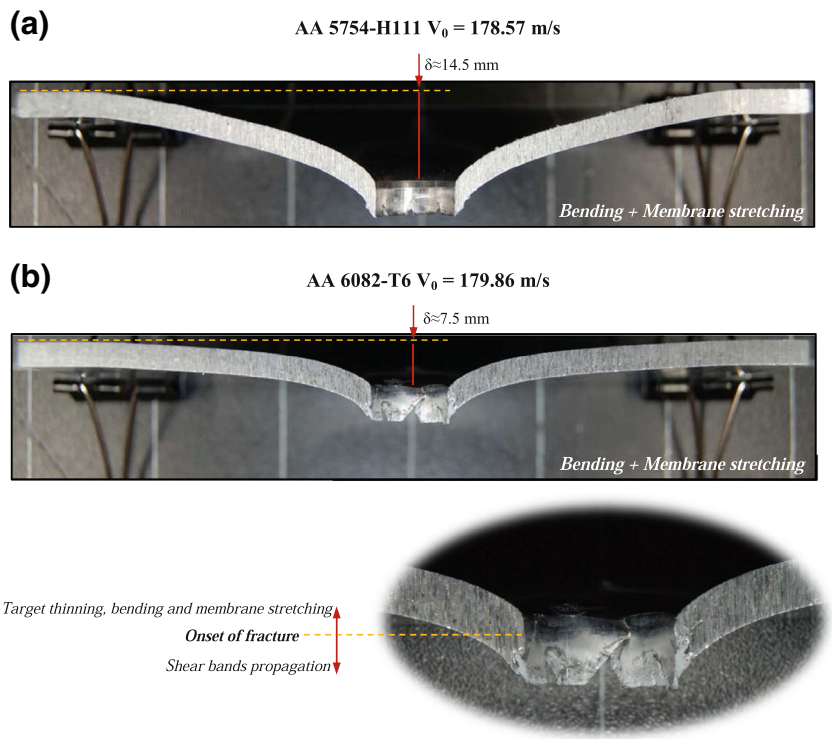

Fig. 12 Hemispherical projectile configuration. Cross-sections of penetrated plates. Both plates are tested at largely similar impact velocities. (**a**) Material: AA 5754-H111. $V_0 = 178.57\ m/s$. (**b**) Material: AA 6082-T6. $V_0 = 179.86\ m/s$

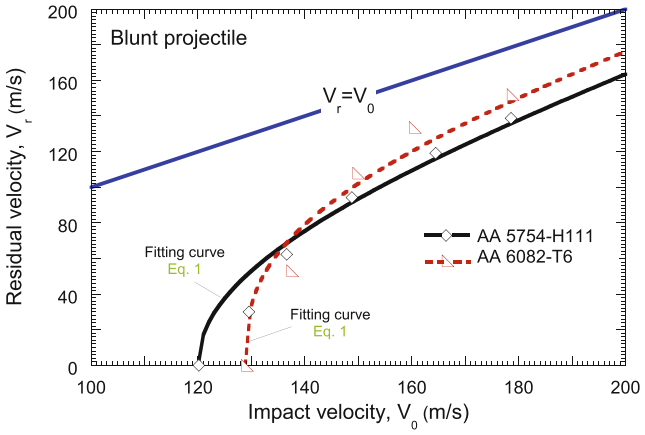

Fig. 13 Blunt projectile configuration. Residual velocity V_r versus impact velocity V_0. Comparison between AA 5754-H111 and AA 6082-T6

velocities the combination of structural and local failure mechanisms displayed by the AA 5754-H111 plates become more energy consuming.

Discussion

This paper examines the influence of projectile nose shape in the normal penetration of 4 mm thickness aluminium targets. Three different projectile configurations have been used: conical, hemispherical and blunt. Two alloys have been considered: AA 5457-H111 and AA 6082-T6. The first one displays low initial yield stress but marked strain hardening and enhanced ductility. The second one shows largely different mechanical response with high initial yield stress, low strain hardening and limited ductility. Such a different mechanical behaviour of the alloys tested facilitates to evaluate the role played by the material in the perforation mechanisms. Thus, the main interest of this study lies in the systematic confrontation of experimental data obtained for two aluminium grades and different projectile configurations. The following points arise from the analysis:

Ballistic Limit

In agreement with experimental, numerical and theoreti-cal observations reported in the literature [18, 49–53] our experiments show the strong influence of the projectile nose shape on the ballistic limit. This relation has been found dependent on the material target as illustrated in Fig. 16. The ballistic limit for the AA 6082-T6 plates continuously decreases throughout the sequence *conical projectile* $\longrightarrow$ *hemispherical projectile* $\longrightarrow$ *blunt projectile* whereas the ballistic limit for the AA 5754-H111 plates shows a relative maximum for the hemispherical penetrator.

Moreover, it has been observed that target strength increase may not lead to ballistic limit decrease in tests using blunt projectiles. This is contrary to other experimental observations reported in the literature (see [53, 54]) which described a decrease in ballistic limit velocity with an increase of target strength when failure is dominated by shear banding. Furthermore, it has been observed that target strength increase may not lead to ballistic limit increase in tests using conical nosed projectiles. This trend is contrary to other experimental observations and empirical models reported in the literature (see [50, 53, 55, 56]) which indicated that there is a monotonic increase in ballistic limit velocity with increasing yield stress when failure is due to ductile hole formation (and contrary to the generally accepted design philosophy, i.e. the higher the strength the better the perforation performance).

Energy Absorption of Target Material

Figure 17 illustrates the energy absorbed by the target E_t calculated by equation (2) versus impact velocity V_0

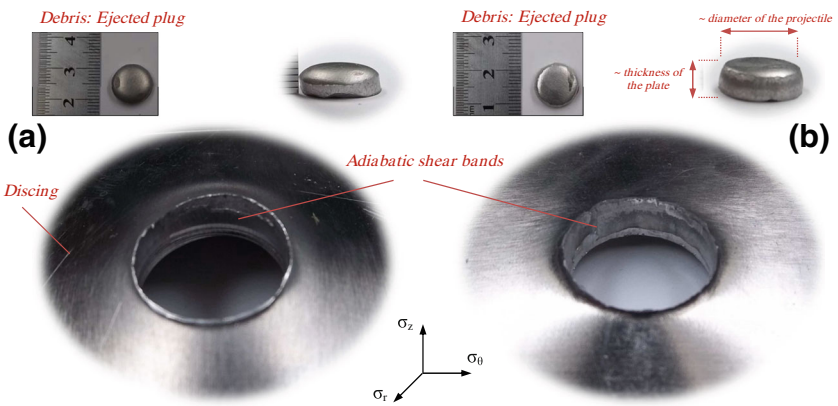

Fig. 14 Blunt projectile configuration. Final stage of the perforation process. (**a**) Material: AA 5754-H111. $V_0 = 136.60\ m/s$. (**b**) Material: AA 6082-T6. $V_0 = 160.26\ m/s$

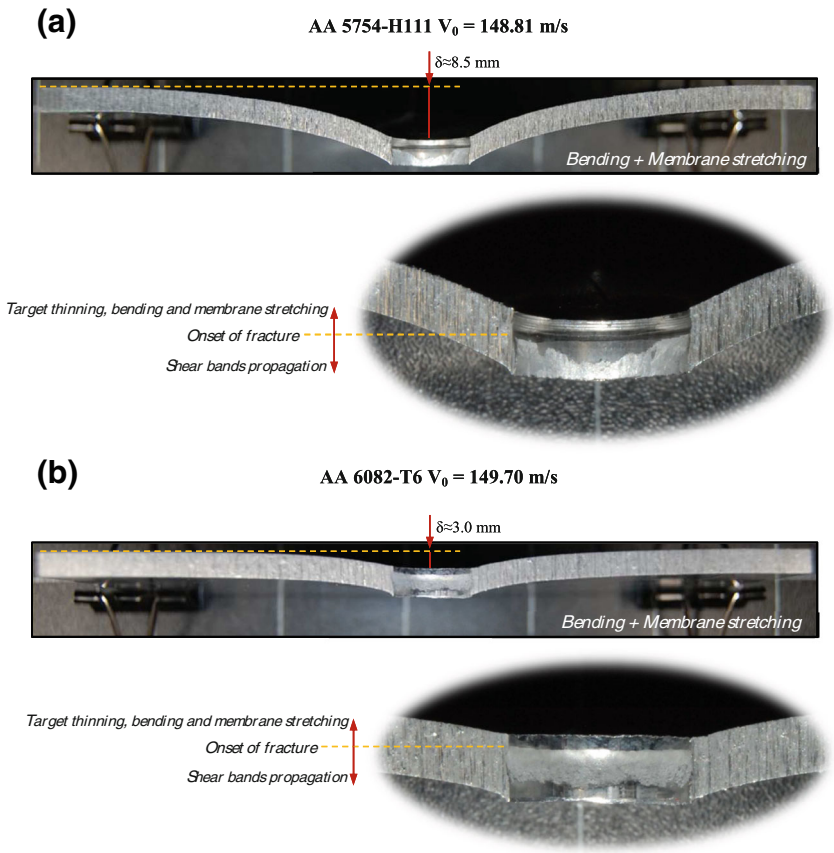

Fig. 15 Blunt projectile configuration. Cross-sections of penetrated plates. Both plates are tested at largely similar impact velocities. (**a**) Material: AA 5754-H111. $V_0 = 148.81\ m/s$. (**b**) Material: AA 6082-T6. $V_0 = 149.70\ m/s$

for the three nose shapes considered and both materials tested.

$$E_t = \frac{1}{2} \cdot M_p \cdot \left(V_0^2 - V_r^2\right) \tag{2}$$

In the case of the AA 5754-H111 plates the hemispherical nosed projectile was found the least effective penetrator within the whole range of impact velocities tested whereas in the case of the AA 6082-T6 targets that was the conical nosed. Interestingly, the latter observation is contrary to experimental results frequently reported in the literature where the hemispherical projectile uses to be identified as the least efficient penetrator. The results shown in this paper may be related to the large flow stress and small strain hardening exhibited by the AA 6082-T6 which makes it prone to develop adiabatic shear bands. This failure mode is characterized by small energy consumption. Namely, the energy required for perforation is that required for the onset of the shear bands. Once the instability is formed the complete penetration of the target is very low energy consuming. Regarding to the particular case of the AA 6082-T6, the nose shape of the hemispherical projectile facilitates the formation of shear bands. This makes the hemispherical projectile more efficient penetrator than the conical one (which does not lead to shear failure of the plate).

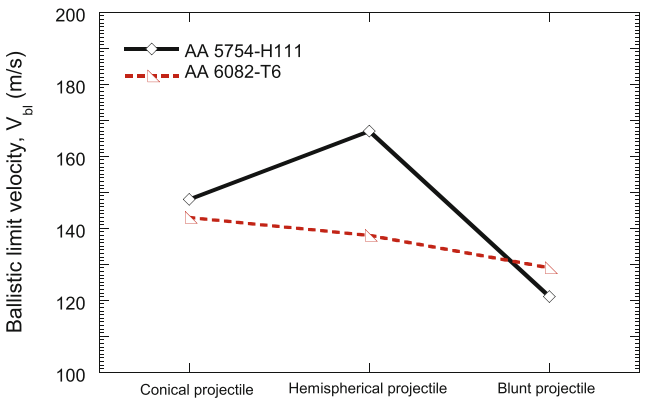

Fig. 16 Ballistic limit velocity V_{bl} versus projectile nose shape for both materials tested

Moreover, it has to be noted that the energy absorbed by the target is largely independent of the impact velocity (within the range of velocities tested) when conical projectiles are used (irrespective of the material target). On the contrary, a marked decrease is observed in the $E_t - V_0$ curves when hemispherical and blunt projectiles are considered.

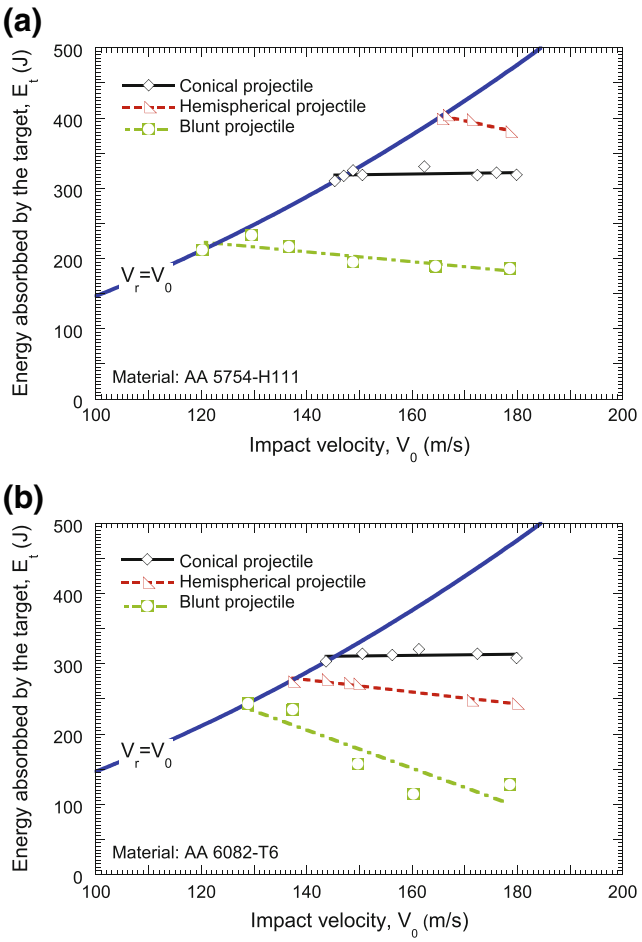

Fig. 17 Energy absorbed by the target E_t versus impact velocity V_0. Comparison between conical, hemispherical and blunt projectiles. (**a**) Material: AA 5754-H111. (**b**) Material: AA 6082-T6

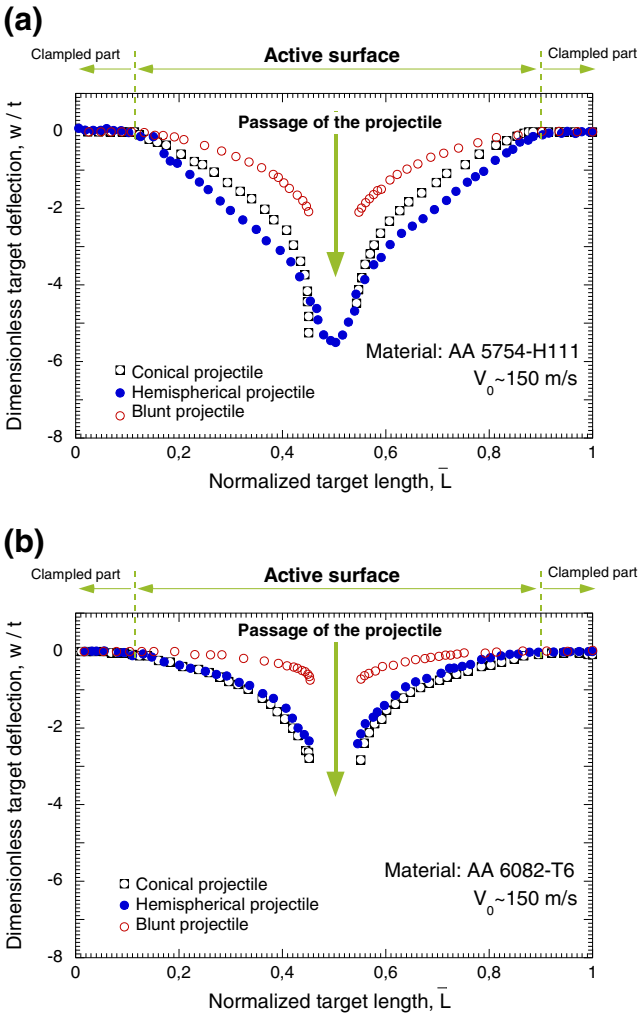

Fig. 18 Dimensionless post-mortem deflection of the plates as a function of the normalized target length. Comparison between conical, hemispherical and blunt projectiles for $V_0 \sim 150\ m/s$. (**a**) Material: AA 5754-H111, (**b**) Material: AA 6082-T6

Perforation Mechanisms

Different failure modes have been observed in the tested samples. These are the result of the respective influence that global (plate deflection, bending and membrane stretching) and local deformations (ductile hole formation, petalling, plugging, rear bulging, discing, tensile tearing, thinning, shear banding and necking) have on the penetration mechanisms.

This distinction between global and local deformations is illustrated in Figs. 18 and 19 where the normalized displacement of the impacted plates w/t (where w is the out-of-plane displacement and t is the target thickness) is shown versus normalized target length $\bar{L}$ for the materials and projectiles considered and two different impact velocities (150 m/s and 180 m/s).

The out-of-plane displacement of the post mortem plates was measured by photographing the profiles of the cross sections using a high-resolution camera. Next, the images were digitalized to obtain the average profile for each plate in accordance with the procedure developed in [57]. Relevant observations can be drawn from this analysis.

General comments:

- For a given material and fixed impact velocity, the plates impacted by blunt projectiles showed much smaller permanent bending that those impacted by conical and hemispherical projectiles.
- For a given impact velocity, the AA 5754-H111 targets show much larger deflection than the AA 6082-T6 plates.
- For a given material, the target deflection increases as the ballistic limit velocity is approached. In other words, the ballistic limit velocity provides the maximum deflection of the plates.

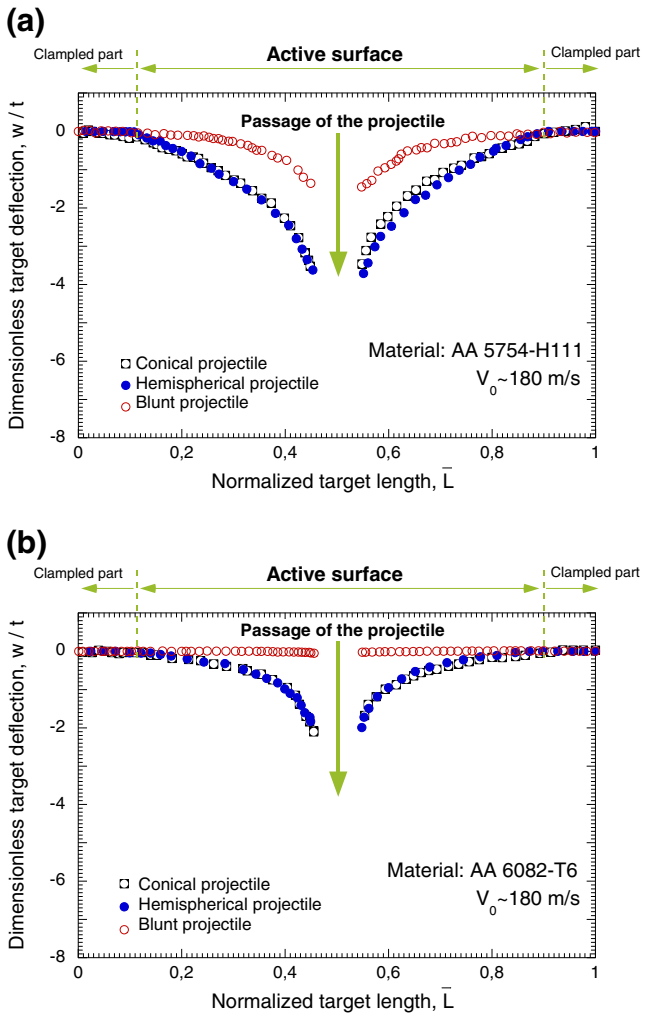

Fig. 19 Dimensionless post-mortem deflection of the plates as a function of the normalized target length. Comparison between conical, hemispherical and blunt projectiles for $V_0 \sim 180\ m/s$. (**a**) Material: AA 5754-H111, (**b**) Material: AA 6082-T6

Specific comments:

- Permanent bending of the AA 6082-T6 plates tested within the highest impact velocities considered ($V_0 \approx 180\ m/s$) is almost negligible when blunt projectiles are used. In such cases the whole energy absorbed by the target seems to be invested on the generation of adiabatic shear bands. Then, the influence of boundary conditions (clamping of the plates) in the penetration process may be neglected.
- Permanent bending of the AA 5754-H111 plates tested at velocities close to the ballistic limit ($V_0 \approx 150\ m/s$) is up to six times the target thickness when conical and hemispherical projectiles are used. In such cases most of the energy absorbed by the target seems to be invested on global deformation mechanisms. Then, the influence of boundary conditions in the penetration process may play a major role. This agrees with the observations reported by Corran et al. [52] who reported that the energy consumed in membrane stretching and bending in thin plates perforated by conical and hemispherical projectiles is higher than that consumed in local deformation mechanisms.

These observations reinforce the idea that the impact energy is absorbed by a combination of local and global deformation mechanisms. Their respective influence in the penetration mechanisms being dependent on: projectile/target configuration, material properties, geometric parameters, boundary conditions and impact velocity.

Conclusions

The experimental results obtained in this paper could be synthesized as follows:

- The ballistic limit measured for the AA 5754-H111 plates is larger than that obtained for the AA 6082-T6 plates when conical and hemispherical projectiles are used. The opposite behaviour is obtained for blunt projectiles.
- Hemispherical projectile is found to be the least efficient penetrator for AA 5754-H111 plates, whereas for the AA 6082-T6 this is the conical projectile. Irrespective of the material considered, blunt projectile was identified as the most effective penetrator.
- Contrary to experimental observations reported in the literature, in this paper has been shown that target strength increase may not lead to decreasing ballistic limit when blunt projectiles are used.
- Contrary to experimental results reported in the literature, in this paper has been shown that increasing target strength may not lead to decreasing ballistic limit when conical projectiles are used.

Acknowledgments The researchers of the University Carlos III of Madrid are indebted to the Comunidad Autónoma de Madrid (Project CCG10-UC3M/DPI-5596) and to the Ministerio de Ciencia e Innovación de España (Project DPI/2011-24068) for the financial support received which allowed conducting part of this work.

J. A. Rodríguez-Martínez thanks Professors R. Zaera and D. Rittel for helpful discussions on dynamic penetration problems.

References

1. Deb A, Mahendrakumar MS, Chavan C, Karve J, Blankenburg D, Storenb S (2004) Design of an aluminium-based vehicle platform for front impact safety. Int J Impact Eng 30:1055–1079
2. Lademo OG, Engler O, Keller S, Berstad T, Pedersen KO, Hopperstad OS (2009) Identification and validation of constitutive

model and fracture criterion for AlMgSi alloy with application to sheet forming. Mater Des 30:3005–3019
3. Mordike BL, Ebert T (2001) Magnesium: properties applications potential. Mater Sci Eng A 302:37–45
4. Nemat-Nasser S, Guo WG, Cheng JY (1999) Mechanical properties and deformation mechanisms of a commercially pure titanium. Acta Materialia 47:3705–3720
5. Nemat-Nasser S, Guo WG, Nesterenko VF, Indrakanti S, Gu YB (2001) Dynamic response of conventional and hot isostatically pressed ti6al4v alloys: experiments and modeling. Mech Mater 33:425–439
6. Miller WS, Zhuang L, Bottema J, Wittebrood AJ, Smet PD, Haszler A (2000) Recent development in aluminium alloys for the automotive industry. Mater Sci Eng A 280:37–49
7. Smerd R, Winkler S, Salisbury C, Worswick M, Lloyd D, Finn M (2005) High strain rate tensile testing of automotive aluminum alloy sheet. Int J Impact Eng 32:541–560
8. Wilson DV (1988) Aluminium versus steel in the family car the formability factor. J Mech Work Technol 16:257–277
9. Chen Y, Pedersen KO, Clausen AH, Hopperstad OS (2009) An experimental study on the dynamic fracture of extruded AA6xxx and AA7xxx aluminium alloys. Mater Sci Eng A 523:253–262
10. Clausen AH, Børvik T, Hopperstad OS, Benallal A (2004) Flow and fracture characteristics of aluminium alloy aa5083h116 as function of strain rate, temperature and triaxiality. Mater Sci Eng A 364:260–272
11. Khan AS, Liu H (2012) Variable strain rate sensitivity in an aluminum alloy: response and constitutive modeling. Int J Plast 36:1–14
12. Langseth M, Hopperstad OS, Hanssen AG (1998) Crash behaviour of thin-walled aluminium members. Thin-Walled Struct 32:127–150
13. Børvik T, Clausen AH, Eriksson M, Berstad T, Hopperstad OS, Langseth M (2005) Experimental and numerical study on the perforation of AA6005-T6 panels. Int J Impact Eng 32:35–64
14. Børvik T, Forrestal MJ, Warren TL (2010) Perforation of 5083-H116 aluminum armor plates with ogive-nose rods and 7.62 mm APM2 bullets. Exp Mech 50:969–978
15. Børvik T, Olovsson L, Dey S, Langseth M (2011) Normal and oblique impact of small arms bullets on AA6082-T4 aluminium protective plates. Int J Impact Eng 38:577–589
16. Forrestal MJ, Børvik T, Warren TL (2010) Perforation of 7075-t651 aluminum armor plates with 7.62 mm APM2 bullets. Exp Mech 50:1245–1251
17. Forrestal MJ, Luk VK, Brar NS (1990) Perforation of aluminum armor plates with conical nose projectiles. Mech Mater 10:97–105
18. Gupta NK, Iqbal MA, Sekhon GS (2006) Experimental and numerical studies on the behaviour of thin aluminium plates subjected to impact by blunt and hemispherical nosed projectiles. Int J Impact Eng 32:1921–1944
19. Gupta NK, Iqbal MA, Sekhon GS (2007) Effect of projectile nose shape, impact velocity and target thickness on deformation behaviour of aluminium plates. Int J Solids Struct 44:3411–3439
20. Gupta NK, Iqbal MA, Sekhon GS (2008) Effect of projectile nose shape, impact velocity and target thickness on the deformation behavior of layered plates. Int J Impact Eng 35:37–60
21. Iqbal MA, Khan SH, Ansari R, Gupta NK (2013) Experimental and numerical studies of double-nosed projectile impact on aluminum plates. Int J Impact Eng 54:232–245
22. Rosenberg Z, Forrestal MJ (1988) Perforation of aluminum plates with conical nosed rods-additional data and discussion. J Appl Mech 55:236–239
23. Børvik T, Clausen AH, Eriksson M, Berstad T, Hopperstad OS, Langseth M (2005) Experimental and numerical study on the perforation of AA6005-T6 panels. Int J Impact Eng 32: 35–64
24. Iwamoto T, Yokoyama T (2012) Effects of radial inertia and end friction in specimen geometry in split hopkinson pressure bar tests: a computational study. Mech Mater 51:97–109
25. Jankowiak T, Rusinek A, Lodygowski T (2011) Validation of the Klepaczko–Malinowski model for friction correction and recommendations on split hopkinson pressure bar. Finite Elem Anal Des 47:1191–1208
26. Oosterkamp L, Ivankovic A, Venizelos G (2000) High strain rate properties of selected aluminium alloys. Mater Sci Eng A 278(1):225–235
27. Winzer R, Glinicka A (2011) The static and dynamic compressive behaviour of selected aluminium alloys. Eng Trans 59:85–100
28. Moćko W, Rodríguez-Martínez JA, Kowalewski ZL, Rusinek A (2012) Compressive viscoplastic response of 6082-T6 and 7075-T6 aluminium alloys under wide range of strain rate at room temperature: experiments and modelling. Strain 48:498–509
29. Rusinek A, Mandrea A, Rebegea S (2010) Wasp sotware for waves analyze. Users Manual, version 1
30. Jovic C, Wagner D, Herve P, Gary G, Lazzarotto L (2006) Mechanical behaviour and temperature measurement during dynamic deformation on split hopkinson bar of 304l stainless steel and 5754 aluminium alloy. J Phys IV 134:1279–1285
31. Wowk DL (2008) Effects of prestrain on the strain rate sensitivity of AA5754 sheet. Ph.D. thesis, Kingston, Ontario
32. El-Magd E, Abouridouane M (2003) Influence of strain rate and temperature on the compressive ductility of al, mg and ti alloys. J Phys IV 110:15–20
33. El-Magd E, Abouridouane M (2006) Characterization, modelling and simulation of deformation and fracture behaviour of the lightweight wrought alloys under high strain rate loading. Int J Impact Eng 32:741–758
34. Franz FA, Duffy J (1972) The dynamic stress-strain behaviour in torsion of 1100-O aluminium subjected to a sharp increase in strain rate. J Appl Mech 39:939–945
35. Kpenyigba K, Jankowiak T, Rusinek A, Pesci R (2013) Influence of projectile shape on dynamic behavior of steel sheet subjected to impact and perforation. Thin-Walled Struct 65:93–104
36. Rodríguez-Martínez JA, Rusinek A, Pesci R, Zaera R (2013) Experimental and numerical analysis of the martensitic transformation in AISI 304 steel sheets subjected to perforation by conical and hemispherical projectiles. Int J Solids Struct 50:339–351
37. Rodríguez-Martínez JA, Rusinek A, Chevrier P, Bernier R, Arias A (2010) Temperature measurements on ES steel sheets subjected to perforation by hemispherical projectiles. Int J Impact Eng 37:828–841
38. Recht RF, Ipson TW (1963) Ballistic perforation dynamics. J Appl Mech 30:384–390
39. Woodward RL (1984) The interrelation of failure modes observed in the penetration of metallic targets. Int J Impact Eng 2:121–129
40. Mercier S, Molinari A (2003) Predictions of bifurcations and instabilities during dynamic extensions. Int J Solids Struct 40:1995–2016
41. Mercier S, Molinari A (2004) Analysis of multiple necking in rings under rapid radial expansion. Int J Impact Eng 4:403–419
42. Rodríguez-Martínez JA, Vadillo G, Fernández-Sáez J, Molinari A (2013) Identification of the critical wavelength responsible for the fragmentation of ductile rings expanding at very high strain rates. J Mech Phys Solids 61:1357–1376
43. Atkins AG, Khan MA, Liu JH (2013) Experimental and numerical analysis of the martensitic transformation in AISI 304 steel sheets

subjected to perforation by conical and hemispherical projectiles. Int J Solids Struct 50:339–351
44. Rodríguez-Martínez JA, Pesci R, Rusinek A, Arias A, Zaera R, Pedroche DA (2010) Thermo-mechanical behaviour of TRIP 1000 steel sheets subjected to low velocity perforation by conical projectiles at different temperatures. Int J Solids Struct 47:1268–1284
45. Rodríguez-Martínez JA, Rusinek A, Arias A (2011) Thermo-viscoplastic behaviour of 2024-T3 aluminium sheets subjected to low velocity perforation at different temperatures. Thin-Walled Struct 49:819–832
46. Rodríguez-Martínez JA, Vadillo G, Zaera R, Fernández-Sáez J (2013) On the complete extinction of selected imperfection wavelengths in dynamically expanded ductile rings. Mech Mater 60:107–120
47. Lee YW, Wierzbicki T (2005) Fracture prediction of thin plates under localized impulsive loading. part ii: discing and petalling. Int J Impact Eng 31:1277–1308
48. Wierzbicki T (1999) Petalling of plates under explosive and impact loading. Int J Impact Eng 22:935–954
49. Børvik T, Langseth M, Hopperstad OS, Malo KA (2002) Perforation of 12 mm thick steel plates by 20 mm diameter projectiles with flat, hemispherical and conical noses part i: experimental study. Int J Impact Eng 27:19–35
50. Backman ME, Goldsmith W (1978) The mechanics of penetration of projectiles into targets. Int J Eng Sci 16:1–99
51. Børvik T, Hopperstad OS, Malo MLKA (2003) Effect of target thickness in blunt projectile penetration of weldox 460 E steel plates. Int J Impact Eng 28:413–464
52. Corran RSJ, Shadbolt PJ, Ruiz C (1983) Impact loading of plates an experimental investigation. Int J Impact Eng 1:3–22
53. Dey S, Børvik T, Hopperstad OS, Leinum JR, Langseth M (2004) The effect of target strength on the perforation of steel plates using three different projectile nose shapes. Int J Impact Eng 30:1005–1038
54. Pereira JM, Lerch BA (2001) Effects of heat treatment on the ballistic impact properties of inconel 718 for jet engine fan containment applications. Int J Impact Eng 25:715–733
55. Aly SY, Li QM (2008) Critical impact energy for the perforation of metallic plates. Nucl Eng Des 238:2521–2528
56. Corbett CG, Reid SR, Johnson W (1996) Impact loading of plates and shells by free-flying projectiles: a review. Int J Impact Eng 18:141–230
57. López-Puente J, Arias A, Zaera R, Navarro C (2005) The effect of the thickness of the adhesive layer on the ballistic limit of ceramic/metal armours. An experimental and numerical study. Int J Impact Eng 32:321–336